Air-sea heat flux climatologies in the Mediterranean Sea: Surface energy balance and its consistency with ocean heat storage

Xiangzhou Song[1,2] and **Lisan Yu[3]**

[1]Physical Oceanography Laboratory, Ocean University of China, Qingdao, China, [2]National Marine Environmental Forecasting Center, State Oceanic Administration, Beijing, China, [3]Department of Physical Oceanography, Woods Hole Oceanographic Institution, Woods Hole, Massachusetts, USA

Abstract This study provides an analysis of the Mediterranean Sea surface energy budget using nine surface heat flux climatologies. The ensemble mean estimation shows that the net downward shortwave radiation (192 ± 19 W m^{-2}) is balanced by latent heat flux (-98 ± 10 W m^{-2}), followed by net longwave radiation (-78 ± 13 W m^{-2}) and sensible heat flux (-13 ± 4 W m^{-2}). The resulting net heat budget (Qnet) is 2 ± 12 W m^{-2} into the ocean, which appears to be warm biased. The annual-mean Qnet should be -5.6 ± 1.6 W m^{-2} when estimated from the observed net transport through the Strait of Gibraltar. To diagnose the uncertainty in nine Qnet climatologies, we constructed Qnet from the heat budget equation by using historic hydrological observations to determine the heat content changes and advective heat flux. We also used the Qnet from a data-assimilated global ocean state estimation as an additional reference. By comparing with the two reference Qnet estimates, we found that seven products (NCEP 1, NCEP 2, CFSR, ERA-Interim, MERRA, NOCSv2.0, and OAFlux+ISCCP) overestimate Qnet, with magnitude ranging from 6 to 27 W m^{-2}, while two products underestimate Qnet by -6 W m^{-2} (JRA55) and -14 W m^{-2} (CORE.2). Together with the previous warm pool work of Song and Yu (2013), we show that CFSR, MERRA, NOCSv2.0, and OAFlux+ISCCP are warm-biased not only in the western Pacific warm pool but also in the Mediterranean Sea, while CORE.2 is cold-biased in both regions. The NCEP 1, 2, and ERA-Interim are cold-biased over the warm pool but warm-biased in the Mediterranean Sea.

1. Introduction

The Mediterranean Sea is located between 30°N and 45°N in the global desert latitudes. The strong dry and cold regional winds in winter generate strong evaporation and latent heat transfer [*Bunker*, 1972; *May*, 1982; *Hellerman and Rosenstein*, 1983], leading to a net heat loss of $\sim$5 W m^{-2} [*MacDonald et al.*, 1994] and a net freshwater loss of $\sim$60 cm [*Mariotti et al.*, 2002; *Mariotti et al.*, 2008; *Pettenuzzo et al.*, 2010] on a yearly bias. The Mediterranean Sea is a semienclosed basin, connected to the Atlantic Ocean in the west by the shallow and narrow Strait of Gibraltar. It is estimated that about 90% of the heat and freshwater losses in the basin are balanced by the warmer and fresher Atlantic waters that enter through the strait [*Bryden and Kinder*, 1991; *Bryden et al.*, 1994; *Tsimplis and Bryden*, 2000; *Candela*, 2001; *Bascheck et al.*, 2001]. The remaining 10% of freshwater loss is supplied by river runoffs (e.g., Po Rhone, Nile, and Ebro) [*Struglia et al.*, 2004].

In the context of the energy and water budget balance, the semienclosed Mediterranean Sea is a constrained basin. It is an ideal location for validating the surface flux estimates against the heat and water budgets that are computed from the hydrographic observations. Many efforts have been made to determine the air-sea exchange on the regional and global scales. However, the energy budgets obtained by various products have not yet reached a balance [*Yu et al.*, 2013]. There is a large spread in the mean averages of surface heat fluxes between products [*Josey et al.*, 2013], most of which are warm-biased that would cause excessive heating to the ocean. This is clearly seen in the application of surface heat flux products to analyze the heat balance in the Mediterranean Sea. For instance, the current nine surface heat flux products (Table 1) suggest an ensemble annual mean heat gain about 2 W m^{-2} (see in section 3.2), which is in sharp contrast to the heat loss diagnosed from the heat transport through the Strait of Gibraltar [e.g., *Bunker et al.*, 1982; *Garrett et al.*, 1993; *Krahmann et al.*, 2000; *Matsoukas et al.*, 2005; *Sanchez-Gomez et al.*, 2011]. The

Table 1. List of the Surface Heat Flux Products and Associated Main Characteristics

Name	Source	Period	Temporal Resolution	Spatial Resolution	Reference
Atmospheric Reanalyses					
NCEP 1	NCEP, NCAR	Jan 1948 onward	6 hourly	1.875° × 1.875°	*Kalnay et al.* [1996]
NCEP 2	NCEP, DOE	Jan 1979 onward	6 hourly	1.875° × 1.875°	*Kanamitsu et al.* [2002]
CFSR	NCEP	Jan 1979 onward	Hourly	0.5° × 0.5°	*Saha et al.* [2010]
ERA-Interim	ECMWF	Jan 1979 onward	6 hourly	0.7° × 0.7°	*Dee et al.* [2011]
JRA-55	JMA	Jan 1958 onward	3 hourly	0.55° × 0.55°	*Kobayashi et al.* [2015]
MERRA	NASA	Jan 1979 onward	3 hourly	0.5° × 0.667°	*Rienecker et al.* [2011]
Analyzed Flux Products					
CORE.2	NOCAR	Jan 1949 to Dec 2006	Monthly	1° × 1°	*Large and Yeager* [2009]
NOCSv2	NOC	Jan 1973 onward	Monthly	1° × 1°	*Berry and Kent* [2009]
OAFlux+ISCCP	WHOI+NASA GISS	Jul 1985 to Dec 2009	Daily + 3 hourly	1° × 1° + 2.5° × 2.5°	*Yu et al.* [2008] and *Zhang et al.* [2004]

numerical weather prediction (NWP) [*Angelucci et al.*, 1998] and the ensemble Regional Climate Models (RCMs) [*Sanchez-Gomez et al.*, 2011] also show major discrepancy with the Gibraltar reference.

The net heat balance (Qnet) at the ocean surface is the sum of the four processes: net downward shortwave radiation (SW), net upward longwave radiation (LW), and turbulent latent heat (LH) and sensible heat (SH) fluxes. The higher estimate of Qnet throughout this paper is termed as "warm bias," as the excessive net downward heating tends to warm up the upper layer of the ocean. Studies attribute the excessive heating bias to either an overestimation of SW by 6.5% [*Garrett et al.*, 1993; *Gilman and Garrett*, 1994], or an underestimation of LW [*Schiano et al.*, 1993; *Gilman and Garrett*, 1994], or weak LH and SH losses at the sea surface [*Bunker et al.*, 1982; *Schulz et al.*, 1997; *Bentamy et al.*, 2003; *Petersen and Renfrew*, 2009]. The underrepresented turbulent heat fluxes in high-wind conditions are particularly noted for the flux climatology constructed from ship reports [*Bunker et al.*, 1982]. Several methods have been proposed to correct the accumulative bias on the total Qnet. One approach was to adjust the mean state of Qnet based on the heat flux advected through the Strait of Gibraltar [*Bethoux*, 1979; *Bunker et al.*, 1982], which is equivalent to -5.2 ± 1.3 W m^{-2} [*MacDonald et al.*, 1994]. The other approach was to use the heat budget simulated from the Ocean General Circulation Models (OGCMs) [*Castellari et al.*, 1998; *Dietrich*, 2004; *Ruiz et al.*, 2008; *Sanchez-Gomez et al.*, 2011].

Concrete progress has been made continuously in improving the quantification of radiative and turbulent heat transfer at the sea surface [*Josey et al.*, 2013]. The latest atmospheric reanalysis efforts have led to four new surface flux products, including the NCEP Climate Forecast System Reanalysis (CFSR) [*Saha et al.*, 2010], NASA's Modern Era Retrospective-analysis for Research and Applications (MERRA) [*Bosilovich*, 2008; *Rienecker et al.*, 2011], the ERA-Interim projects [*Dee and Uppala*, 2009], and the Japan Meteorological Agency (JMA) 55 year Reanalysis (JRA-55) [*Kobayashi et al.*, 2015]. These latest versions feature improved spatial and temporal resolutions, an enhanced use of satellite observations from 1979 onward, and the state-of-the-art data assimilation schemes. However, to what degree the latest reanalysis efforts have improved the representation of surface heat exchange processes and the energy budget balance on both regional and global scales is yet fully assessed.

This study seeks to address two objectives. One is to provide an evaluation of the state of the surface energy balance in the Mediterranean Sea determined from the surface heat flux climatologies that are currently available. In particular, the degree of the spread in the estimates of each of the air-sea exchange process (i.e., SW, LW, LH, and SH) will be analyzed. The other objective is to examine the physical consistency of the surface heat flux climatologies with the observationally based ocean heat storage. The latter will be used as a reference to help diagnose and quantify the bias in the flux climatologies. Although the study is on the regional scale, it is the second part of our concerted efforts toward a systematic evaluation of the structure and magnitude of the uncertainties in the Qnet climatologies over the global scale. In the first part of the study [*Song and Yu*, 2013; hereinafter SY13], we established a framework to examine the physical consistency of nine flux climatologies in the western Pacific warm pool with ocean temperature observations. By using the observed ocean heat budget together with in situ air-sea and subsurface measurements, we provided a quantification of the statistical uncertainty in the surface energy budget estimate over the world's warm waters. The dynamical framework of the heat budget analysis in the Mediterranean Sea is different

from that in the SY13 in two major perspectives. The first and most distinct difference lies in that the Mediterranean Sea is a semienclosed sea, and the budget integration is performed in a fixed ocean basin that has complex coastlines and topography. Second, the Mediterranean Sea is located in the global dessert zone, influenced strongly by dry and cold northern winds in the winter. The basin has a net heat loss on the annual mean basis, unlike the western Pacific warm pool that has a net heat gain throughout the year. Therefore, the Mediterranean budget analysis will provide valuable insights into the uncertainty structure and characteristics of the present heat flux estimates in regions beyond the tropics. To better connect with the SY13 work, the same products are used in this study except for the replacement of ERA-40 with JRA-55. ERA-40 suffers from various deficiencies and the surface budget is apparently in error. JRA-55 was not available at the time of writing SY13.

The paper is organized as follows: section 2 describes the data sets and methodology. Section 3 presents the analysis of the surface heat budget balance. Section 4 provides the diagnosis of the discrepancies in the products based on the integrated ocean heat storage equation. Summary and discussion are given in section 5.

2. Methodology and Data Sets

2.1. Formulation of the Dynamical Framework

The strong evaporation in the Mediterranean Sea results in a freshwater loss of 50–100 cm/yr [*Bethoux*, 1979; *Bryden and Kinder*, 1991; *Bryden et al.*, 1994; *Tsimplis and Bryden*, 2000; *Candela*, 2001; *Bascheck et al.*, 2001; *Mariotti et al.*, 2002, 2008; *Pettenuzzo et al.*, 2010] and a heat loss of 4–7 W m^{-2} [*Bunker et al.*, 1982; *MacDonald et al.*, 1994]. The net evaporation loss, together with the conservation of mass and salt, drives a two-layer exchange flow through the Strait [*Bryden and Stommel*, 1984]. In the upper layer fresh and warm Atlantic water flows into the basin through the Strait of Gibraltar, while in the lower layer a compensating flow of colder and saltier water exits from the basin toward the Atlantic. On the time-mean basis, the gain of advective heat transport through the Strait of Gibraltar should be compensated by a heat drain through the air-sea heat fluxes. Thus, the Gibraltar heat exchange provides a strong constraint on the estimates of the heat flux at the air-sea interface.

The primitive heat budget equation can be written as

$$\frac{\partial T}{\partial t} + \nabla_h(uT) = \frac{1}{\bar{\rho}\,\bar{c_p}}\nabla \cdot (Qnet) - k_h \cdot \nabla_h^2\,T, \qquad (1)$$

where T is the temperature, u the horizontal velocity vector, $\bar{\rho}$ the averaged density, $\bar{c_p}$ the basin-averaged specific heat capacity, and k_h the horizontal eddy coefficient for the diffusive heat. In equation (1), the four terms from left to right denote the rate of change in temperature, horizontal heat advection, surface heat flux divergence, and the horizontal heat diffusion, respectively. The vertical advection and diffusion are not included, as the integration is performed over the entire Mediterranean Sea. There are other potential heat sources, but all are deemed small. For instance, the geothermal heat flux from the ground is generally weak and considered negligible [*Stein and Stein*, 1992, 1994; *DeLaughter et al.*, 2005]. The heat influx from the Black sea, which is estimated to be less than 1 W m^{-2} [*Garrett et al.*, 1993], is considered negligible [*Tolmazin*, 1985]. It is also assumed that the lateral and bottom boundaries are thermally insulated when computing the basin-integrated heat budget.

At the Strait of Gibraltar, only the zonal velocity (along-strait) is considered. By integrating equation (1) over the entire Mediterranean Sea and applying the Gaussian theorem to the terms of advection, surface heat flux divergence, and diffusion, one yields

$$\underbrace{\frac{\partial}{\partial t}\int_v Tdv}_{\text{Term I}} + \underbrace{\int_{s_1} uTdA_1}_{\text{Term II}} = \underbrace{\frac{1}{\bar{\rho}\,\bar{c_P}}\int_s QnetdA}_{\text{Term III}} - \underbrace{k_h\int_{s_1}\nabla_h TA_1}_{\text{Term IV}}, \qquad (2)$$

where s_1 denotes the cross section of the Strait, s the entire surface of the Mediterranean Sea, with A_1 and A being the respective integral area. In equation (2), all terms can be computed from existing data sets. The heat storage term (Term I) are computed from the given ocean temperature fields. The annual mean advection term (Term II) are estimated by using a baroclinic transport (0.81 ± 0.07 Sv for the upper layer and

-0.76 ± 0.07 Sv for the lower layer) through the Strait of Gibraltar [*Bascheck et al.*, 2001]. However, for the seasonal variations, the advective heat flux is calculated in reference to the climatological monthly transport by *Soto-Navarro et al.* [2010]. Term III are estimated from existing surface flux climatologies. Term IV is determined from the zonal temperature gradient between the temperature profiles in and out of the Strait, with the horizontal eddy coefficient k_h set at 2000 m^2 s^{-1}. On the time-mean basis, the loss of the surface heat flux (Term III) is compensated by the heat input through the Strait (Term II), and the net heat residual in the basin is close to zero. However, the errors in flux climatologies are usually so large that they are not able to balance the budget as suggested [*Gilman and Garrett*, 1994; *Sanchez-Gomez et al.*, 2011]. Hence, the heat budget residual in equation (2) has been used as a tool to quantify the errors in the surface flux climatologies. This is also an approach used in the following analysis.

2.2. Description of Data Sets

As mentioned, two sets of data information are needed in equation (2). One is the subsurface temperature climatology and the other is the surface flux climatology. The subsurface temperature climatology is taken from the World Ocean Atlas 2009 (WOA09) [*Locarnini et al.*, 2010], which is the average of the decadal means over the five periods: 1955–1964, 1965–1974, 1975–1984, 1985–1994, and 1995–2006. Other data sets, such as the MEDAR/MEDATLAS project [*Fichaut et al.*, 2003], also provide choices for the calculation of the heat storage change (Term I). This study is the second part of our efforts toward better understanding and quantification of the uncertainties in the global flux climatologies [*Song and Yu*, 2012; SY13]. The WOA09 is chosen as the reference data set in our efforts because it can be applied on both regional and global scales. In using the WOA09 in this study, the vertical profile of the temperature fields was linearly interpolated into 1 m resolution. Heat content at each grid was computed by the multiplication of the temperature and the geophysical volume at the grid point. The monthly heat content over the basin was further interpolated into daily values so that the monthly heat storage rate was presented by the heat content differences between the last 5 day mean and the first 5 day mean of the month.

Due to the uncertainty in surface flux estimates, one single data set is not sufficient to characterize the range of uncertainty. Hence, a total of nine flux products were used. Two products are from the first and second generations of atmospheric reanalyses, including the National Center for Environmental Prediction/National Center for Atmospheric Research (NCEP/NCAR; hereafter NCEP 1) reanalysis [*Kalnay et al.*, 1996] and NCEP/Department of Energy (NCEP/DOE; hereafter NCEP 2) reanalysis [*Kanamitsu et al.*, 2002]. Four latest atmospheric reanalysis products are used, including CFSR, ERA-interim, JRA55, and MERRA. The three analyzed Qnet products are the Objectively Analyzed Air-sea Flux (OAFlux) [*Yu and Weller*, 2007; *Yu et al.*, 2008] plus the surface radiation from the International Climatology Cloud Project (ISCCP) [*Zhang et al.*, 2004], the National Oceanography Centre, Southampton version 2.0 (NOCSv2.0) [*Berry and Kent*, 2009, 2011], and the version 2 forcing for Common Ocean-ice Reference Experiments (CORE.2) [*Large and Yeager*, 2009]. Key characteristics of the nine products are summarized in Table 1. The three analyzed products (OAFlux, NOCSv2.0, and CORE.2) have 1° × 1° resolution, while the others were interpolated onto the same grids to facilitate the computation. A monthly climatology was constructed for the 20 year period from 1987 to 2006.

Besides the above nine climatologies, the Qnet and SW climatology can also be provided by ocean data assimilation models, such as the project of Estimating the Circulation & Climate of the Ocean (ECCO) [*Wunsch and Heimbach*, 2007]. The SW in ECCO is a control variable using the ERA-Interim as the initial condition. The other flux terms are computed from the bulk flux algorithm [*Large and Yeager*, 2004] and the output is not provided. We include the ECCO surface Qnet and SW as an additional reference here, because these estimates are from an ocean model that satisfies both ocean dynamics and data constraints. The newly released 20 year (1982–2011) ECCO version [*Forget et al.*, 2015] is used, in which the Qnet and SW are gridded on a 0.5° × 0.5° horizontal resolution.

3. Mean and Seasonal Variability of Surface Heat Flux Climatologies and Associated Uncertainties

3.1. Ensemble Mean and Spread of the Annual-Mean Qnet and Heat Flux Components

The ensemble annual mean Qnet is obtained from averaging the nine Qnet climatologies (Figure 1a). The mean Qnet is characterized by a heat loss over the Gulf of Lyon, the Adriatic and Aegean Seas, and a heat
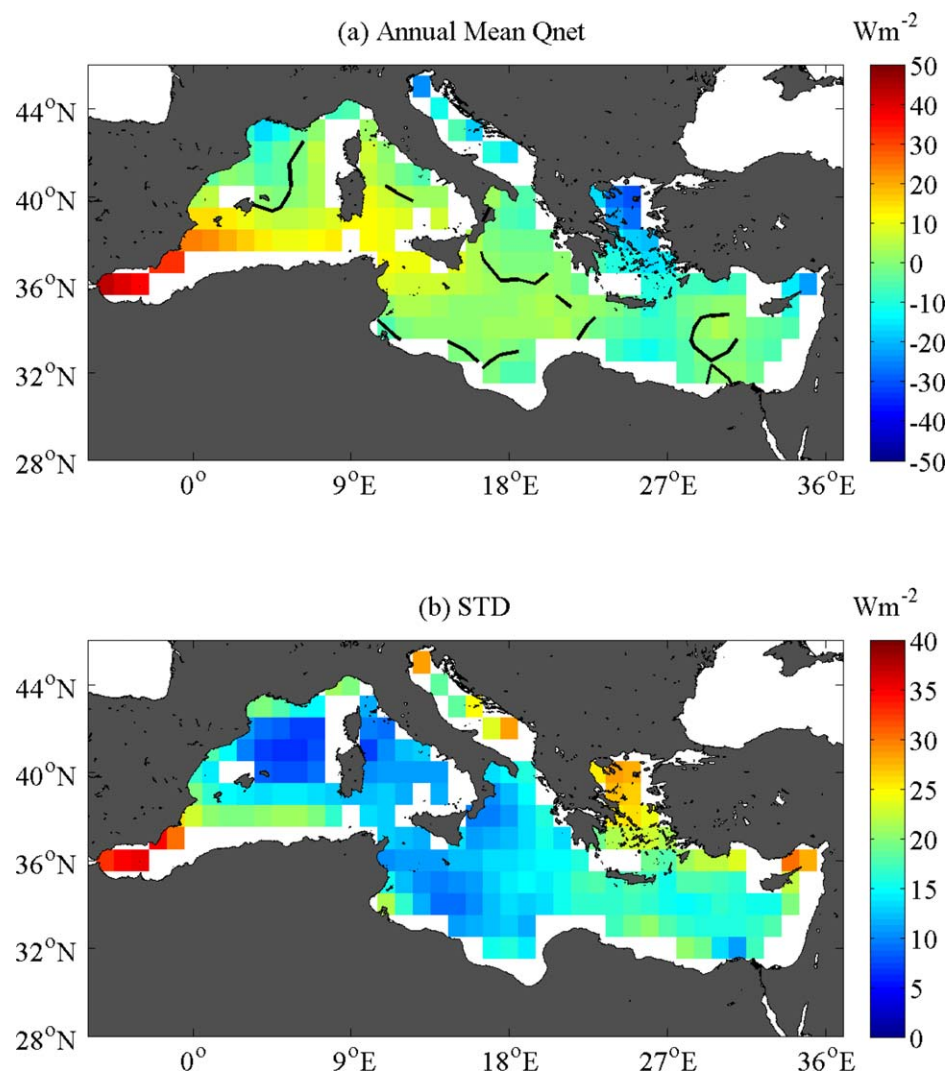
Figure 1. (a) Spatial distribution of the ensemble mean of the Qnet in the Mediterranean Sea averaged over nine climatologies. Positive values denote downward heat flux (i.e., the sea surface receives heat from the atmosphere), while negative values denote upward heat flux (i.e., the sea surface loses heat to the atmosphere). The solid lines represent the zero-contour of the Qnet. (b) STD (spread) of the nine Qnet mean climatologies.

gain over the Alboran Sea, the interior of the Western (WM) and Eastern Mediterranean (EM). On an annual basis, the Mediterranean Sea gains heat in the south but loses heat in the north, influence by the wintertime wind pattern that blows cold and dry continental air from north downward to the south. The high evaporation and strong surface cooling in the northwestern Mediterranean Sea (NM) [*MEDOC Group*, 1970; *Sankey*, 1973; *Madec et al.*, 1991] and the Eastern Mediterranean [*Plakhin*, 1972; *Sultan et al.*, 1987] lead to the deep convection and the formation of the dense water. The maximum heat loss is approximately 30 W m^{-2} in the Gulf of Lyon. On the other hand, the maximum heat gain is roughly 50 W m^{-2} in the Alboran Sea, where the air-sea humidity contrast is small and the wind is relatively weak. The ensemble annual-mean Qnet averaged over the basin is 2 ± 12 W m^{-2}. Given that the oceanographic observations at the Strait of Gibraltar indicate an annual-mean loss of -5.2 ± 1.3 W m^{-2} [*MacDonald et al.*, 1994], the ensemble mean of Qnet is largely warm-biased.

The nine Qnet climatologies are not all consistent with each other, and their differences are quantified using the standard deviation (STD) (Figure 1b). The STD (spread) in the nine products is relatively smaller in the WM than that of the EM. In the latter, the STD spread exceeds 20 W m^{-2} on average, with the largest value of ~30 W m^{-2} in the Aegean Sea. The spread in Qnet is less than 10 W m^{-2} in the NM deep water
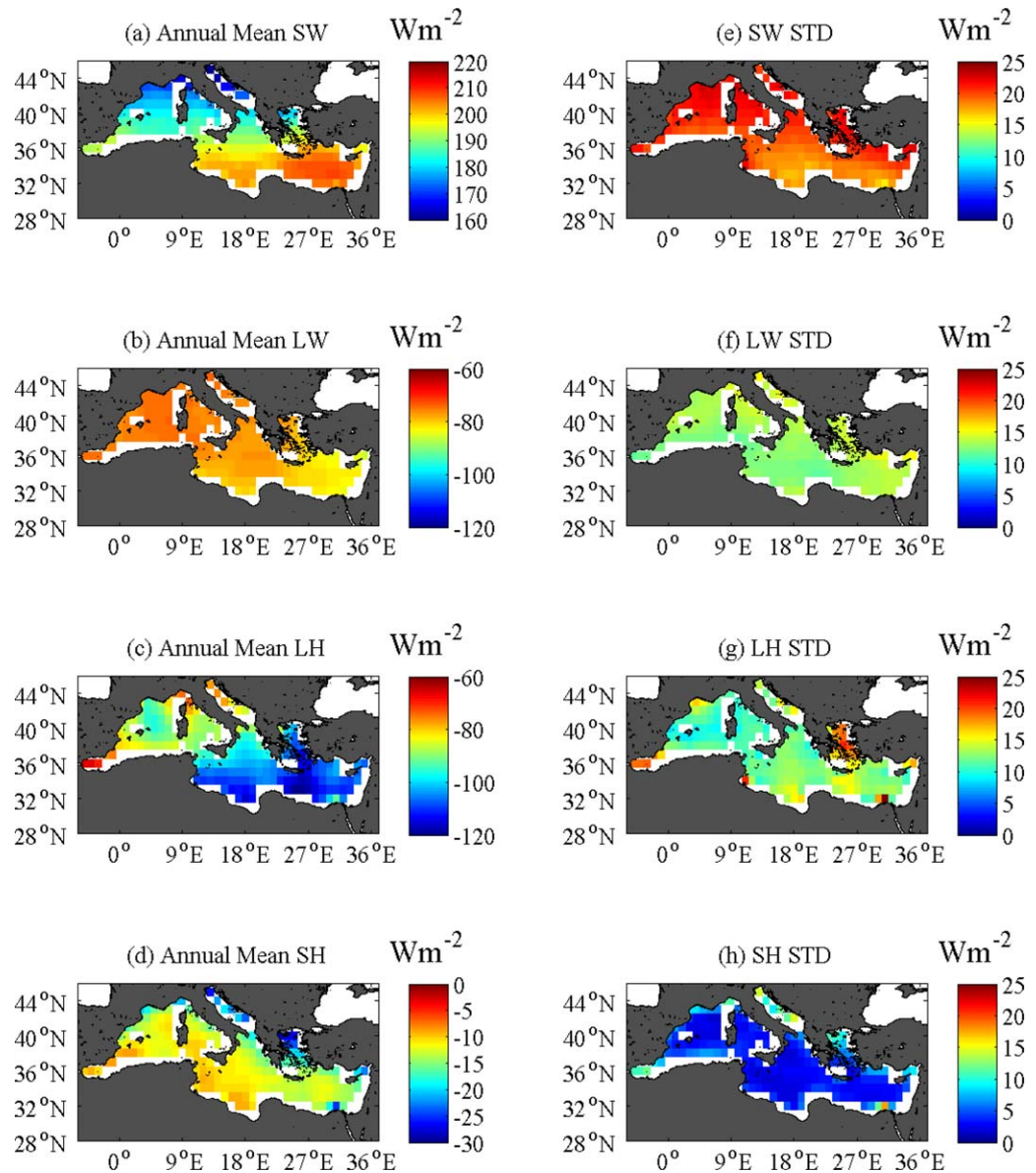
Figure 2. Spatial distribution of the ensemble mean (a) SW, (b) LW, (c) LH, and (d) SH constructed from nine climatologies. The STD (spread) of the nine mean climatologies (e) SW, (f) LW, (g) LH, and (h) SH.

formation region. The ensemble mean spread in Qnet is 12 W m^{-2} when averaged over the basin, accounting for 6 times of the ensemble mean Qnet.

The ensemble annual mean fields of the four heat flux components, net SW, net LW, LH, and SH (Figures 2a–2d), and their respective STD spread (Figures 2e–2h) are constructed. The net SW shows a gradual decrease from north to south due to the variation of the solar zenith angle with latitude. The net solar gain exceeds 200 W m^{-2} in the southeastern basin, while is below 170 W m^{-2} in the NM. The net LW decreases from -74 W m^{-2} in the southeast to -86 W m^{-2} in the northwest (Figure 2b), with an average of -78 W m^{-2} over the basin. The EM basin is generally more evaporative, and the LH loss reaches 120 W m^{-2} south of the Aegean Sea (Figure 2c). The SH loss is higher in the coastal region (Figure 2d), due to the strong air-sea thermal contrast caused by the cold continental winds. In the interior basin, the SH is relatively smaller, less than 10 W m^{-2}.

The differences in the SW products (Figure 2e) care the major cause of the spread in the Qnet products, followed by the contributions from LW (Figure 2f), LH (Figure 2g), and SH (Figure 2h). The STD of SW (Figure

2e) is near uniformly large at 21 W m^{-2} in the northern basin north of 34°N, while south of this latitude, the spread is reduced slightly to 19 W m^{-2}. The pattern of the SW STD distribution is opposite to the pattern of the mean SW (Figure 2a), suggesting that the nine climatologies experience more difficulty in determining the magnitude of solar radiation in the northern basin where the mean SW is comparably smaller than the southern basin.

Although different bulk formula can result in discrepancies for the SW calculation, previous studies have shown that SW is overestimated due to the lack of seasonal and spatial variability of aerosols and water vapor density [*Bunker*, 1972; *Garrett et al.*, 1993; *Gilman and Garrent*, 1994; *Schiano*, 1996; *Castellari et al.*, 1998; *Tragou and Lascaratos*, 2003]. In particular, *Tragou and Lascaratos* [2003] performed a systematic long-term comparison of the solar heat flux estimated from a cloud reduction bulk formula [*Reed*, 1977] with the ground truth observations that were obtained at the coastal meteorological stations over the basin. They showed that SW is systematically overestimated by 25 W m^{-2} for a period of 30 years, and the overestimation occurs mostly during summer in clear-sky conditions. The lack of spatial and temporal variations of the attenuation due to aerosols and, possibly, to water vapor absorption, is suggested as a plausible explanation for the uniformly overestimated SW. We suspect this to be a reason for the large spread in the nine SW climatologies examined here. Similar to the effect of the aerosols, the clouds at the sea surface can also reduce the net solar radiation by reflecting a significant amount of radiation back to the space and trapping the radiation in the cloudy atmosphere [*Ramanathan et al.*, 1989, 1995]. Different reanalyses have different cloud parameterizations, and so the reanalyzed net SW products (e.g., NCEP and ERA-Interim) do not converge at the sea surface. The satellite-derived ISCCP net SW was estimated from the cloud-radiative models [e.g., *Zhang et al.*, 2004], and the CORE.2 is based on the ISCCP.

The spread in the LW, LH, and SH products increases toward the coastal region. The same problem is also found in the high-resolution regional climate models [*Sanchez-Gomez et al.*, 2011], which is attributed to the complex topography related oceanic and atmospheric processes [*Samuel et al.*, 1999]. The STDs (Figures 1b and 2f–2h) are largest in the Adriatic Sea when compared to the STDs in the other parts of the basin. The integrated STD around the Mediterranean coast for LW, LH, and SH is 14, 15, and 6 W m^{-2}, respectively, contrasting to their values of 10, 10, and 5 W m^{-2} in the interior.

3.2. Surface Energy Budget and Uncertainties

The basin-averaged mean and STD for the Qnet and four flux components were constructed for each of the nine climatologies and are summarized in Table 2. Values in the parentheses denote the seasonal STD. The ensemble mean and STD spread of the nine climatologies are also complied (Table 3). The STD in Table 3 refers to the STD of the mean across the nine climatologies. Except for JRA-55 and CORE.2 that have a net heat loss, all the other seven products show a net heat gain, with Qnet ranging from 1 W m^{-2} by NCEP 1 to 21 W m^{-2} by MERRA. The seven Qnet estimates are obviously warm biased, and the bias in MERRA is exceptionally large. The Qnet in JRA-55 is -12 W m^{-2} and Qnet in CORE.2 is -19 W m^{-2}, both of which have the right sign but are 2–3 time stronger in magnitude compared to the observed estimate of -5.2 ± 1.3 W m^{-2} [*MacDonald et al.*, 1994]. The STD Qnet in all products is strong, ranging between 93 W m^{-2} (NOCSv2.0) and 133 W m^{-2} (NCEP 2). The ensemble mean of the nine Qnet products yields a heat gain of 2 W m^{-2} (Table 3), which is obviously warm-biased.

Table 2. Basin-Averaged Annual-Mean Budget of Qnet (Unit: W m^{-2}) and Four Individual Components, SW, LW, LH, and SH (Unit: W m^{-2})[a]

Name	Qnet	SW	LW	LH	SH
NCEP 1	1 ($\pm$116)	191 ($\pm$75)	-79 ($\pm$2)	-97 ($\pm$31)	-14 ($\pm$14)
NCEP 2	9 ($\pm$133)	216 ($\pm$89)	-83 ($\pm$1)	-111 ($\pm$34)	-12 ($\pm$15)
CFSR	8 ($\pm$119)	207 ($\pm$83)	-85 ($\pm$2)	-105 ($\pm$27)	-10 ($\pm$10)
ERA-interim	7 ($\pm$114)	198 ($\pm$81)	-84 ($\pm$2)	-95 ($\pm$27)	-11 ($\pm$10)
JRA-55	-12 ($\pm$109)	198 ($\pm$77)	-79 ($\pm$6)	-112 ($\pm$25)	-19 ($\pm$9)
MERRA	21 ($\pm$122)	203 ($\pm$80)	-89 ($\pm$7)	-82 ($\pm$23)	-11 ($\pm$7)
CORE.2	-19 ($\pm$117)	182 ($\pm$76)	-81 ($\pm$9)	-101 ($\pm$23)	-19 ($\pm$14)
NOCSv2	4 ($\pm$93)	149 ($\pm$61)	-45 ($\pm$3)	-88 ($\pm$27)	-12 ($\pm$6)
OAFlux+ISCCP	3 ($\pm$124)	185 ($\pm$79)	-76 ($\pm$4)	-93 ($\pm$34)	-13 ($\pm$15)

[a]Not that Qnet = SW+LW+LH+SH. The values in the parentheses denote the seasonal STD.

Table 3. Ensemble Mean and STD Spread of the Mean Constructed From Nine Climatologies (Unit: W m^{-2})

Name	Qnet	SW	LW	LH	SH
Mean	2	192	−78	−98	−13
Spread	12	19	13	10	4

On an annual basis, the heat content change in the basin should be zero. With a net input of 2 W m^{-2}, the basin-integrated heat budget cannot achieve a heat budget balance unless the horizontal heat diffusivity (Term IV in equation (2)) through Strait could be as large as −7.2 W m^{-2} to balance out the surface excessive heat (Term III) and the heat advection (Term II in equation (2)). However, since the horizontal temperature gradient is small and the horizontal eddy diffusive coefficient cannot be much higher than 2000 m^{-2} s^{-1} [*Gent and McWilliams*, 1990], the horizontal diffusivity is estimated to be roughly at 3×10^{-3} W m^{-2}. Given the residual warm bias of 7.2 W m^{-2}, we can conclude that the Qnet of the nine-climatology ensemble is overestimated.

Differences in SW are large (Table 2), with the lowest insolation of 149 W m^{-2} from NOCSv2.0 and the highest insolation of 216 W m^{-2} from NCEP 2. The seasonal variability (STD) ranges from 61 (NOCSv2.0) to 89 (NCEP 2) W m^{-2}. Apparently, NCEP2 has both the largest mean and the strongest seasonal variability. Likewise, NOCSv2.0 has the smallest mean and the weakest seasonal variability. The basin-averaged ensemble mean of the nine SW climatologies is 192 W m^{-2} (Table 3), and the STD spread of 19 W m^{-2} accounts for about 10% of the mean SW.

The nine LW climatologies differ by a factor of 2 in the mean, with the weakest estimate of −45 W m^{-2} from NOCSv2.0 and the largest estimate of −89 W m^{-2} from MERRA. It is worth noting that, except for NOCSv2.0, the LW estimates from the other eight climatologies are rather close. The basin-averaged ensemble mean of the nine LW products is −78 W m^{-2}, with a STD spread of 13 W m^{-2} (Table 2). The largest STD spread is located in the southeast basin (Figure 2f).

The nine LH products vary between −112 and −82 W m^{-2}. The LH estimates from JRA-55 (−112 W m^{-2}) and NCEP 1 (−111 W m^{-2}) are at the higher end, while those from MERRA (−82 W m^{-2}) and NOCSv2.0 (−82 W m^{-2}) are at the lower end. The ensemble mean is −98 W m^{-2}, with a STD spread of 10 W m^{-2}. The mean SH is comparably smaller, with the nine SH climatologies ranging between −19 and −10 W m^{-2}. The large estimate is from JRA-55 and CORE.2 while the low estimate from CFSR. The ensemble mean is −13 W m^{-2}, with a STD spread of 4 W m^{-2} (Table 3).

As shown in Tables 2 and 3, the net SW (192 W m^{-2}, downward) is balanced predominantly by net LW (−78 W m^{-2}, upward) and latent heat loss (−98 W m^{-2}, upward), while the contribution of sensible heat loss (−13 W m^{-2}, upward) is small, accounting for less than 7%. To quantify the partition between the flux components more clearly, the bar maps of the nine climatologies are shown (Figure 3a). Two features are noted. First, MERRA is the only product that shows the LW loss is larger than LH, while all other eight products indicate that LH is the dominant heat loss term, followed by LW and SH. Second, NOCSv2.0 has the lowest estimate in all three main components, SW, LW, and LH, showing that the weaker insolation is accompanied by also weaker LW and LH loss. The resulting net heat balance is of 4 W m^{-2}, which is higher than NCEP1, JRA-55, CORE.2, and OAFlux+ISCCP.

It is not yet clear from Figure 3a how the sum of the four terms in JRA-55 and COAR.2 ends up with a net heat loss, with a magnitude that is 2–3 times larger than the budget inferred from the oceanographic data [*MacDonald et al.*, 1994]. To gain a deeper insight, two additional sets of scatterplots are made. The first scatterplot shows the partition between surface radiative components (SW+LW) and turbulent heat loss −(LH+SH) (Figure 3b). For JRA-55 and CORE.2, the SW+LW are less than the –(LH+SH), that is, the net radiative input is less than the net turbulent heat loss. Interestingly, although a net heat loss is achieved by both products, CORE.2 (SW+LW) is about 20 W m^{-2} lower in (SW+LW) and about 10 W m^{-2} lower in –(LH+SH) when compared to JRA-55. For the other seven climatologies, (SW+LW) is larger than –(LH+SH), which causes a net heat gain.

The second scatterplot measures the ratio between (SW+LW) and –LH (Figure 3c). In the tropical and subtropical oceans, the LH was found to be the dominant component in balancing the incoming SW [*Nigam and Chao*, 1996; *Carton and Zhou*, 1997; *Yu*, 2007; *Foltz et al.*, 2010]. There is also an indication (Table 2) that the intensity of LH relative to the intensity of SW+LW may determine the sign of Qnet. This is seen that the weak LH and strong SW in MERRA lead to a large positive Qnet at 21 W m^{-2}. On the other hand, the weak
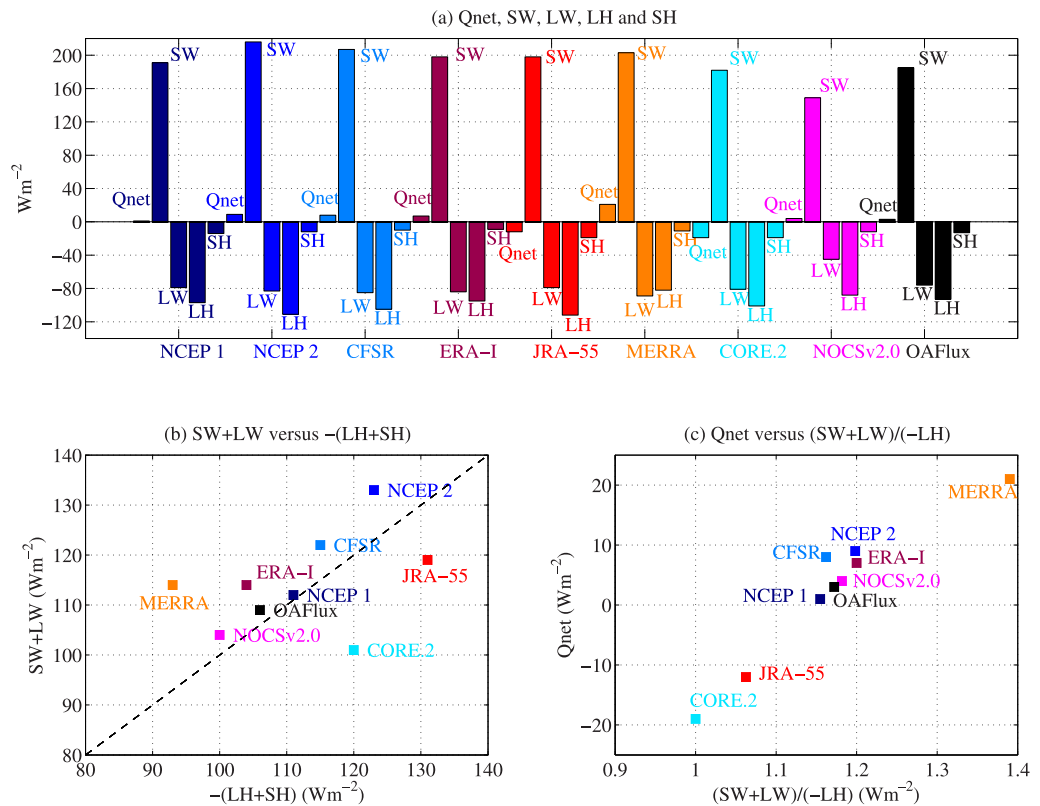
Figure 3. (a) Bar plot of basin averages of Qnet, SW, LW, LH, and SH for the nine products. (b) Scatterplot of SW+LW versus −(LH+SH). (c) Scatterplot of (SW+LW)/(−LH) versus Qnet.

SW but large LH in CORE.2 yields a large negative Qnet at −19 W m^{-2}. As shown in Figure 3c, the threshold of the ratio, (SW+LW)/−LH, could be set at 1.1 to get the right sign of Qnet. When the ratio is less than 1.1 but greater than 1, such as the case for JRA-55 and CORE.2, Qnet is negative. By comparison, when the ratio is greater than 1.1 but less than 1.2, such as the case for the six climatologies (NCEP 1, 2, CFSR, ERA-Interim, NOCSv2.0, and OAFlux+ISCCP), Qnet is positive but less than 10 W m^{-2}. When the ratio approaches 1.4 such as MERRA, Qnet exceeds 21 W m^{-2}, which is the highest among all the nine climatologies.

3.3. Dominant Processes in the Seasonal Variations of Qnet

Seasonal variability of Qnet and four flux components (Figures 4a–4e) is examined to identify the dominant source of discrepancies in Qnet on seasonal timescales. Albeit the amplitude differs, all Qnet climatilogies display a similar seasonal cycle (Figure 5a) that is synchronous with the seasonal cycle of SW (Figure 5b). All SW climatologies also agree with each other on the seasonal cycle, except for NOCSv2.0, which is weaker and has the seasonal peak shifted 1 month later to July. The other eight SW climatologies all have a peak in June and July, when the solar zenith angle is largest. Qnet is positive in the boreal spring/summer from April to August, when SW excesses the heat loss induced by LW, LH, and SH. However, in the boreal fall/winter from October to February of the following year, the total heat loss (LW+LH+SH) surpasses SW which leads to a negative Qnet. For the 2 months, March and September, Qnet is near zero.

The nine LH and SH climatologies (Figures 4d and 4e) show a similar feature: they largely agree on the seasonal cycle but differ in magnitude. JRA-55 has the strongest latent and sensible heat loss, mostly noted in the summer months from May to September. NOCSv2.0 has 1 month shift in the cycle. By comparison, LW from the nine climatologies has large deviations from each other not only in magnitude but also in seasonal variations (Figure 4c). The LW of NOCSv2.0 is weaker than the other eight climatologies, about 30 W m^{-2} in magnitude (magenta line in Figure 4c). As the SW of NOCSv2.0 is also weak (Figure 4b), the term of SW+LW is comparable to the other climatologies. On the annual mean state, the SW+LW of NOCSv2.0 is larger than
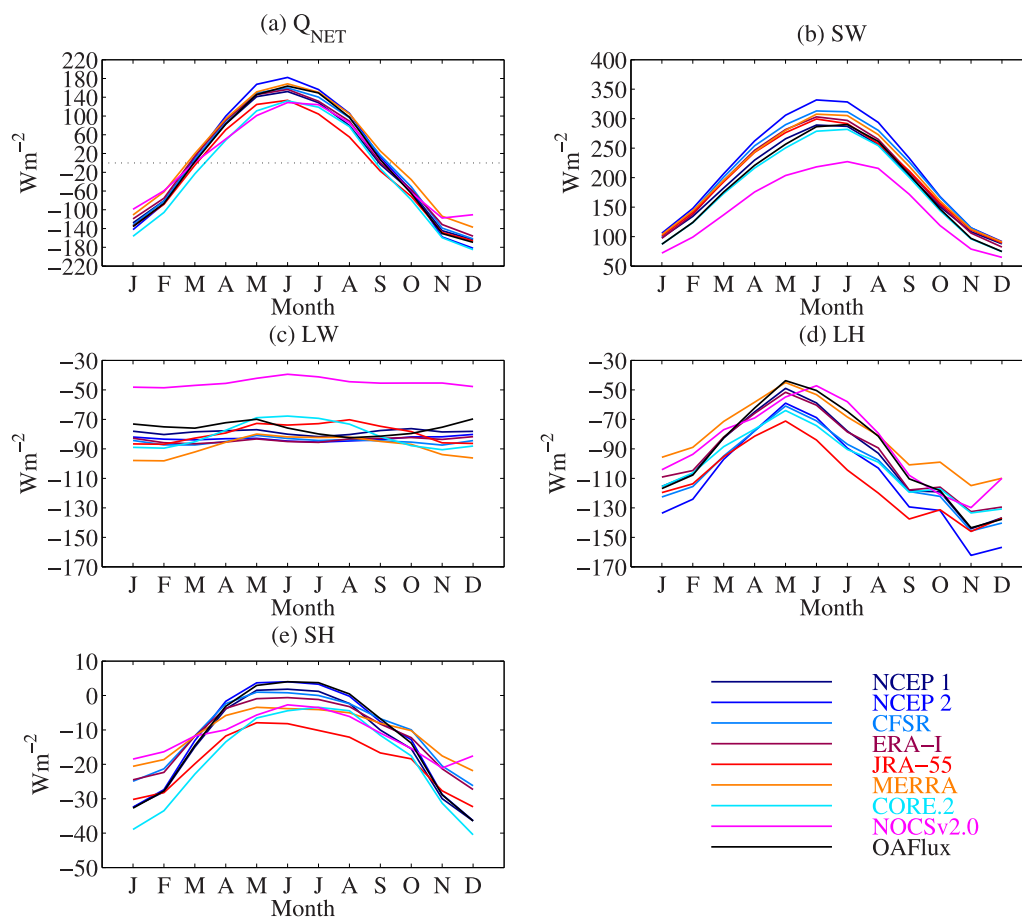
Figure 4. Seasonal variations of (a) Qnet, (b) SW, (c) LW, (d) LH, and (e) SH. Positive values denote downward heat transfer, while negative values denote upward heat transfer. Note the *y* axis of SH in Figure 4e is different from that of the other two loss terms of (c) LW and (d) LH.

the term of −(LH+SH) (see in Figure 3b), which causes a warm bias in Qnet. The most peculiar seasonal pattern of LW is depicted by CORE.2, showing that LW and SW have a similar seasonal cycle, both with a peak in June and July. All other LW products agree more or less with each other on semiannual cycles, with the first peak in May and the second peak in late fall, although the exact timing of the second peak varies considerably with products.

The nine-climatology averaged seasonal cycles of Qnet and the four components with the error bars superimposed are constructed (Figures 5a–5e). The error bars represent 2σ, that is, two times of the STD spread of the nine climatologies. The errors are significant at 95% level. Qnet are positive in spring and summer (March–September) and negative in fall and winter (September–March of the following year). The Qnet STD spread increases when the magnitude of Qnet is larger in summer and winter (Figure 5a). Interestingly, the STD spread of SW is also largest in summer when there is less cloud (Figure 5b), while the STD spread of turbulent heat fluxes (LH and SH, Figures 5d and 5e) is largest in winter when strong air-sea thermal/humidity differences are larger and winds are stronger. Winds play an equivalent role as the air-sea humidity/thermal contrast in determining LH and SH [*Yu*, 2007; *Song and Yu*, 2012]. The large spread in LH is attributable to be the differences in winds.

The sea surface SW is closely associated with the cloud radiative effects [*Hartmann and Doelling*, 1991; *Chen et al.*, 2000] and aerosol effects [*Tragou and Lascaratos*, 2003]. The accuracy of the SW climatologies is sensitive to the parameterizations in the radiative energy models. It is worth noting that CORE.2 SW is from ISCCP SW but applied a global reduction of 5% [*Large and Yeager*, 2009]. There is a subjective 5% magnitude difference between CORE2.0 SW and OAFlux+ISCCP SW.
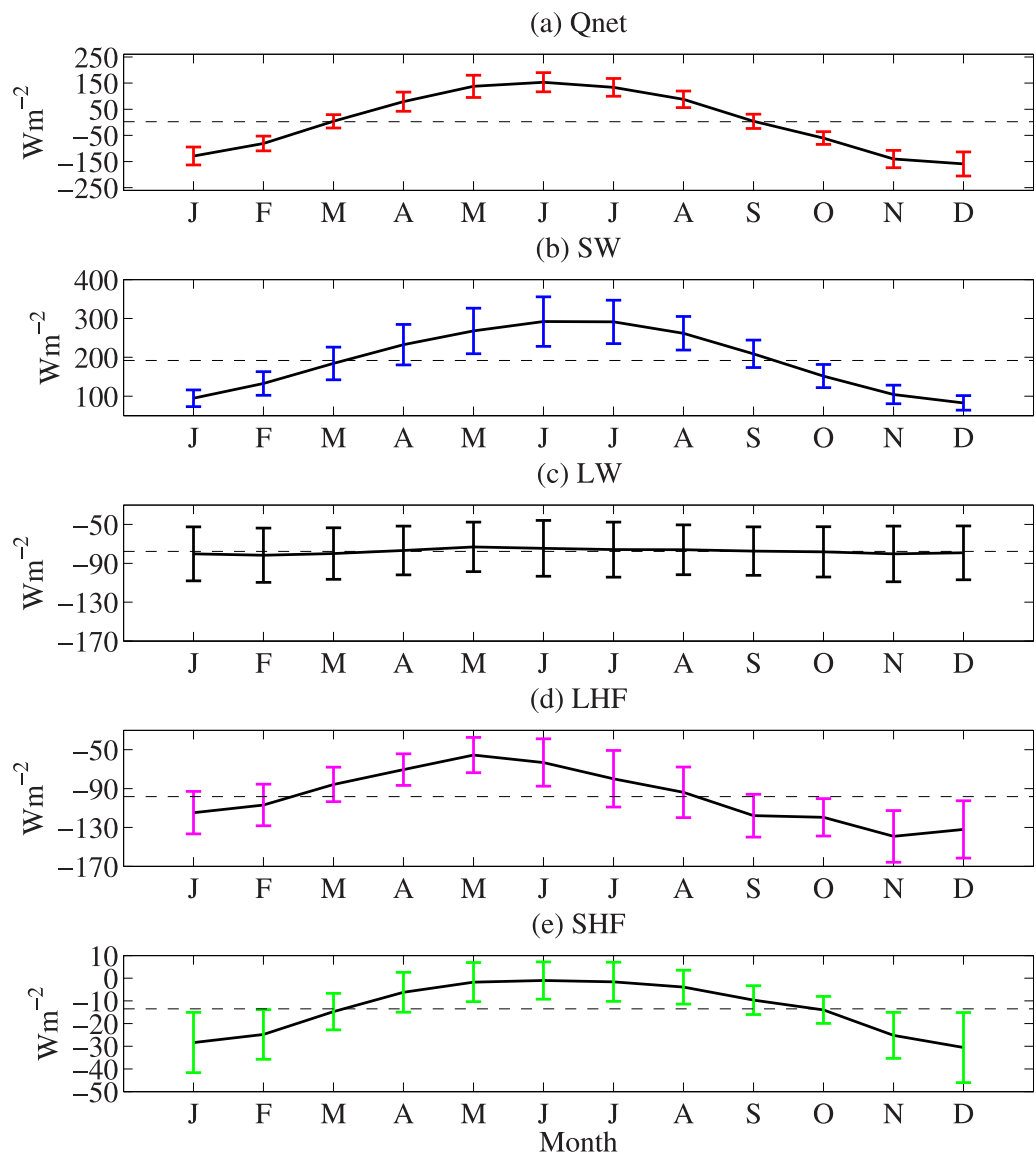
Figure 5. Seasonal variations of surface budgets averaged over nine climatologies (a) Qnet, (b) SW, (c) LW, (d) LH, and (e) SH over the Mediterranean Sea. The error bars are significant at 95% level (2σ). Dashed lines denote the mean value of the flux components.

The ensemble seasonal cycle of the nine LW climatologies shows smaller seasonal variation, unlike the other three components (SW, LH, and SH). However, the STD spread for the ensemble LW is large, reflecting the major uncertainty in estimating the heat fluxes in the Mediterranean Sea is LW. A study by *Bignami et al.* [1995] showed the LW based on the bulk formula is underestimated about 30 W m^{-2} compared to the in situ direct measurements of infrared budget in the Mediterranean Sea. The calculation based on the infrared budget bulk formulas was summarized by *Fung et al.* [1984]. The cloud effects and water vapor in the lower atmosphere can potentially introduce the large errors to net LW, which should be considered separately in different cases. Besides, different schemes of bulk formulas [*Fung et al.*, 1984] can lead to a major difference of about 60 W m^{-2} between the highest and lowest estimates.

4. Heat Budget Analysis

4.1. Basin-Integrated Heat Budget Analysis

Terms in equation (2) were calculated. The annual mean of the Term I reaches a zero balance. The seasonal variation of Term I was presented by the difference of the heat content between the last 5 day mean and
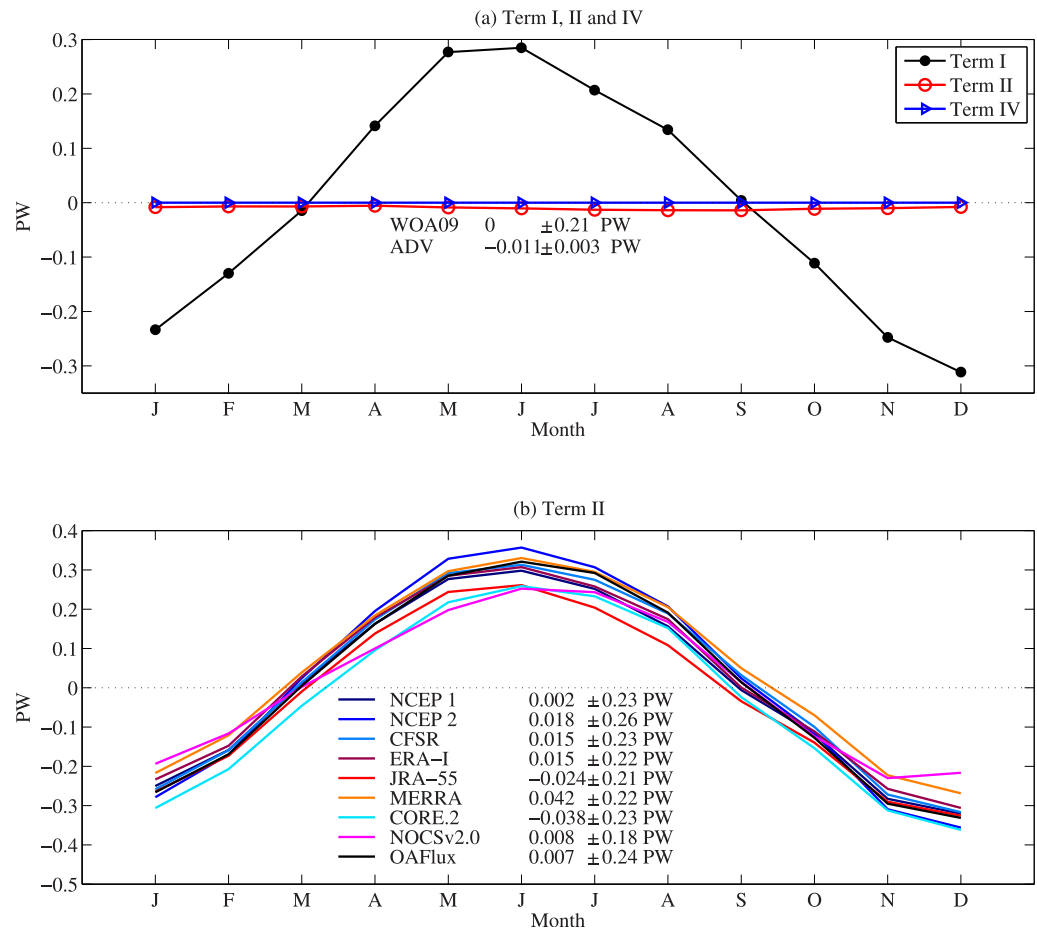
Figure 6. (a) Seasonal variations of Term I (line with solid circle), Term II (red line with empty circle), and Term IV (blue line with triangle) of equation (2). (b) Term III in equation (2) from nine climatologies. Numbers below the curves are the mean total heat budget of Term III for each product.

the first 5 day mean in a given month. The daily heat content was obtained by interpolating the monthly data into daily values. On an annual mean state, the baroclinic transport was taken to be 0.81 ± 0.07 Sv for the upper layer and -0.76 ± 0.07 Sv for the lower layer [*Bascheck et al.*, 2001]. The interface depth for the inflow and outflow was chosen to be 180 m according to both in situ observations [*Soto-Navarro et al.*, 2010] and model results [*Bascheck et al.*, 2001]. *Soto-Navarro et al.* [2010] analyzed 5 year in situ observations and showed that the annual mean inflow and outflow are 0.81 ± 0.06 Sv and -0.78 ± 0.05 Sv, respectively, but with significant annual and semiannual variations [*Lafuente et al.*, 2002]. The inflow peaks in September, while the outflow in magnitude peaks in April. The climatological monthly inflow, outflow, and interface depth in this paper were set to be the values provided by *Soto-Navarro et al.* [2010, Figure 6].

Term II is estimated as follows:

$$\int_{S_1} uTdA_1 \cong \overline{V}\,\overline{T} = \overline{V}_{up}\int_{-180}^{0} Tdz + \overline{V}_{dn}\int_{bottom}^{-180} Tdz, \tag{3}$$

where $\overline{V}$ and $\overline{T}$ represent the section-integrated volume transport and temperature, $\overline{V}_{up}$ and $\overline{V}_{dn}$ denote the upper and lower layer volume transport. The annual mean of Term II was estimated at -0.011 PW (Figure 6a, 1 PW $= 1 \times 10^{15}$ W) with a seasonal STD 0.003 PW. The integrated diffusive heat flux (Term IV) at the cross section of the Strait only quantifies 3×10^{-6} PW (Figure 6a) using a constant horizontal diffusivity 2000 m^2 s^{-1}. Therefore, on an annual mean state, the advective heat flux of -0.011 PW (Term II) should be only compensated by Qnet (Term III). Therefore, the annual mean of Term III ($\frac{1}{\rho\,c_p}\int QnetdA$) should be -0.011 PW. Dividing the energy of -0.011 PW by the surface area, the Qnet is -5.6 W m^{-2}, indicating a

heat loss. Due to the lack of long-term high spatial and temporal resolutions of velocity and temperature profiles, the uT in equation (3) is represented by the mean of $\overline{uT}$ without considering the perturbation term $\overline{u'T'}$. However, it is believed that the term of $\overline{u'T'}$ is a smaller contribution to the advective heat flux [*MacDonald et al.*, 1994]. The seasonal variability of the advective flux does exist (Figure 6a). The Term II peaks in September at -7.2 W m^{-2} when the warm inflow is intensive, but minimized to be -2.8 W m^{-2} when the cold outflow is strong in April.

The seasonal variations of the Terms I and II are balanced by Term III. However, the seasonal STDs of Terms I and III are much larger than their means and Term II (Figure 6), which indicates a strong annual cycle (Figures 4a and 5a). The scales of equation (2) are dominated by Terms I and III for the seasonal variability, which is the balance between the heat storage rate and Qnet. From April to August when the solar radiation is stronger (Figures 4b and 5b) in the Northern Hemisphere, the basin-integrated Qnet is positive and the excessive heat will be stored by increasing the ocean heat content, while from October to February of the following year, the accumulated heat content is released to the atmosphere by intensive turbulent latent and sensible heat loss from the ocean surface (Figures 4d, 4e, 5d, and 5e). In March and September, Term I is approximately zero because Qnet in these 2 months is near zero. MERRA has the highest surface energy with an annual mean at 0.042 PW. Its seasonal STD is 0.22 PW, nearly 5 times than the annual mean. CORE.2 has the lowest energy of -0.038 PW with the seasonal STD of 0.23 PW. The other seven climatologies range from -0.024 PW (JRA-55) to 0.018 PW (NCEP 2).

4.2. The Reconstructed Qnet and Error Analysis

The heat budget analysis allows the mean and seasonal Qnet to be reconstructed inversely using Terms II and I. In equation (3), the along-strait transport was set at 0.81 Sv for the upper layer and -0.76 Sv for the lower layer [*Bascheck et al.*, 2001]. However, the estimates can differ [*Bryden and Kinder*, 1991; *Bryden et al.*, 1994; *Tsimplis and Bryden*, 2000; *Candela*, 2001; *Soto-Navarro et al.*, 2010]. The transport errors for the upper and lower layer were from the STD of the values that have been published, which are 0.12 and 0.13 Sv, respectively. Equation (4) is used to quantify the error for Term II

$$\sigma_{Term\ II} = \frac{\overline{\rho c_P}\left(\int_{s1}\overline{u}\sigma_T dA1 + \int_{s1}\sigma_u\overline{T}dA1\right)}{s}, \qquad (4)$$

where σ_u denotes the error of the along-strait velocity, σ_T represents the statistical error of WOA09 temperature climatology, the other symbols are the same as that in equation (2). The first term on the RHS of equation (4) is roughly one sixth of that of the second term, as the σ_T is only 1/30 of the mean temperature $\overline{T}$. That is to say, the main error is ascribed to be the along-strait transport uncertainty. The error of in $\sigma_{Term\ II}$ in equation (4) is estimated to be 0.8 W m^{-2}. Therefore, the advective heat flux is 5.6 ± 1.6 W m^{-2}, which is significant at 95% confidence level.

The seasonal Qnet is inversely reconstructed by estimating the heat content changes and seasonal advective heat flux (red curve in Figure 7a). The maximum and minimum reconstructed Qnet is in June and December, which is 140 W m^{-2} and -163 W m^{-2}, respectively. The Qnet is -11 and -5 W m^{-2} in March and September. The statistical errors from the WOA09 temperature give rise to a mean error of 10 W m^{-2} for the reconstructed Qnet by

$$\sigma_{Term\ I} = \frac{\overline{\rho c_P}\left(\frac{d}{dt}\int_v \pm\sigma_T dv\right)}{s}. \qquad (5)$$

Therefore, the mean total error ($\sqrt{\sigma_{Term\ I}^2 + \sigma_{Term\ II}^2}$) for the reconstructed Qnet is 10 W m^{-2} (red error bars in Figure 7a) on average, and is significant at 95% confidence level. This error is mainly introduced by the WOA09 statistical errors rather than the advective heat flux.

4.3. ECCO Qnet and SW

The mean Qnet in ECCO is -6 W m^{-2}, equivalent to the annual mean Qnet from the WOA09 estimate. On the seasonal basis, ECCO has a Qnet maximum of 166 W m^{-2} in June and a minimum of -186 W m^{-2} in December, with a Qnet at 8 W m^{-2} in March and -33 W m^{-2} in September. The statistical errors for the seasonal climatology are larger in winter but smaller in summertime (blue line in Figure 7a). The annual cycle of net SW shows a maximum of 292 W m^{-2} in June and a minimum of 78 W m^{-2} in December (Figure 7b). The seasonal variation of ECCO Qnet (blue) is stronger than that of the reconstructed Qnet (red) from
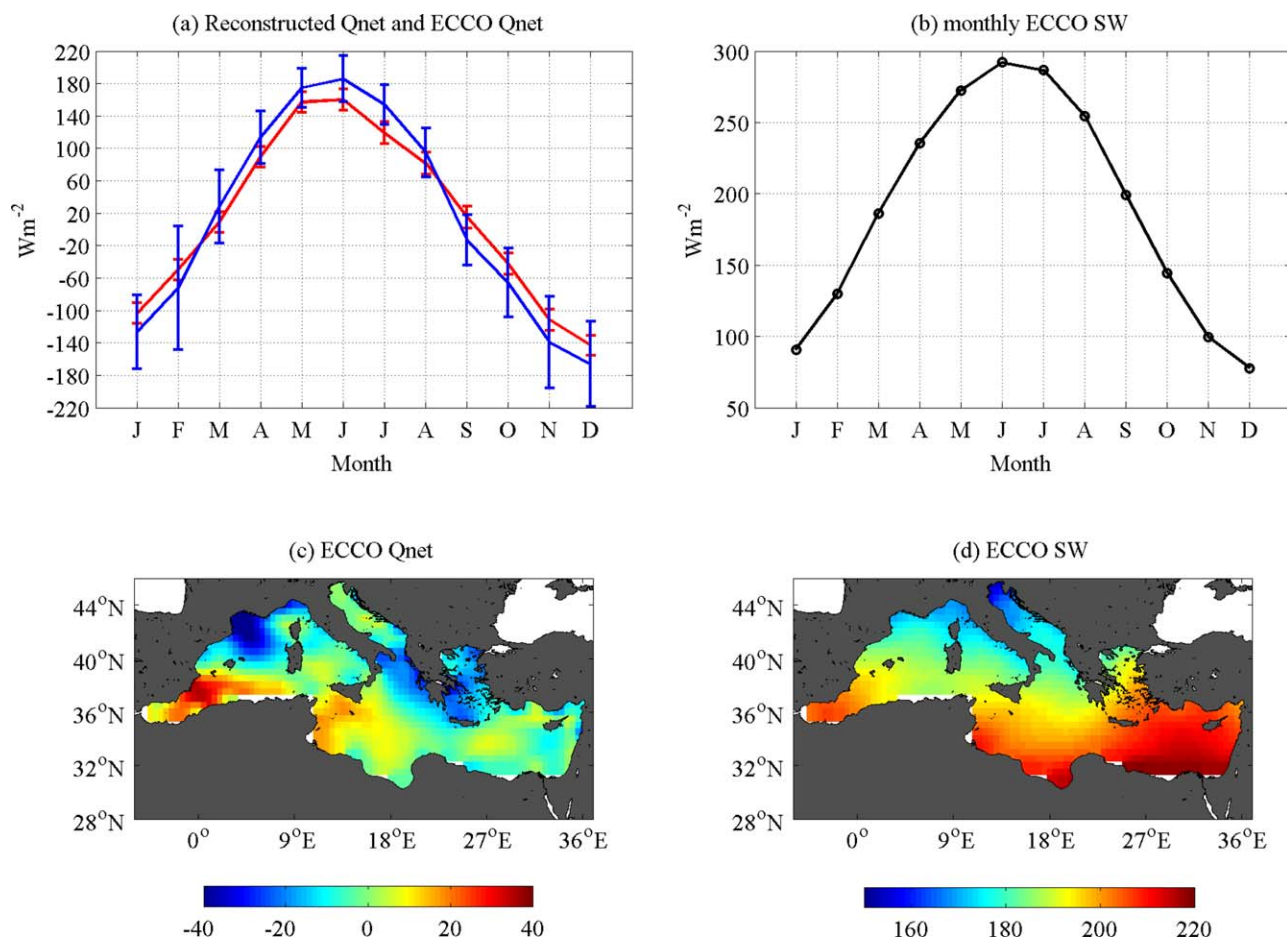
Figure 7. (a) The reconstructed Qnet from WOA09 (unit: W m^{-2}, red) versus the ECCO Qnet in ECCO (blue). Error bars are derived from statistical analysis. (b) The seasonal evolution of the net SW in ECCO. (c) Spatial distribution of ECCO Qnet. (d) The same as Figure 7c, but for net SW.

WOA09. For the basin-scale integration, the sampling density and quality may be an issue for WOA09 due to the lack of sufficient data coverage on monthly basis. ECCO synthesize model physical with an extremely diverse set of observations, including SST, sea level from satellite, and in situ profiles from ARGO. Thus, the climatological seasonal Qnet of ECCO is potentially better represented than that of the WOA09, albeit it is yet to be demonstrated.

The annual mean pattern of the Qnet in ECCO (Figure 7c) is similar to that of the 9-product ensemble mean Qnet (Figure 1a). However, the ECCO Qnet is much more negative than the ensemble mean Qnet (Figure 1a) in the northwestern Mediterranean Sea. The maximum Qnet in ECCO is 36 W m^{-2} over the Mediterranean Sea occurs in Alboran Sea, while the minimum is -47 W m^{-2} in the Gulf of Lyon. Compared to the ensemble mean, the ECCO Qnet has more heat loss than heat gain. The ECCO SW (Figure 7d) show that the maximum SW is 219 W m^{-2} in the southern Levantine basin, and the minimum is 154 W m^{-2} in the northern Adriatic Sea. The mean SW is 189 W m^{-2}, 3 W m^{-2} less than the ensemble mean SW (Table 3). A clear advantage of ECCO Qnet and SW is the resolution. The 0.5° resolution model data have more ocean grids that can depict the Mediterranean coastline better than 1° resolution. The ECCO heat flux is bale to capture the topography-related oceanic and atmospheric processes, and their complex interactions.

4.4. Intercomparison of ECCO/WOA09 With the Nine Climatologies

The reconstructed Qnet from WOA09 (Figure 6) is used to evaluate the annual-mean Qnet from the nine climatologies. A warm bias is seen in a number of products, including NCEP 1 ($+6$ W m^{-2}), NCEP

(a) Annual mean Qnet difference with seasonal STD (nine climatologies – ECCO)

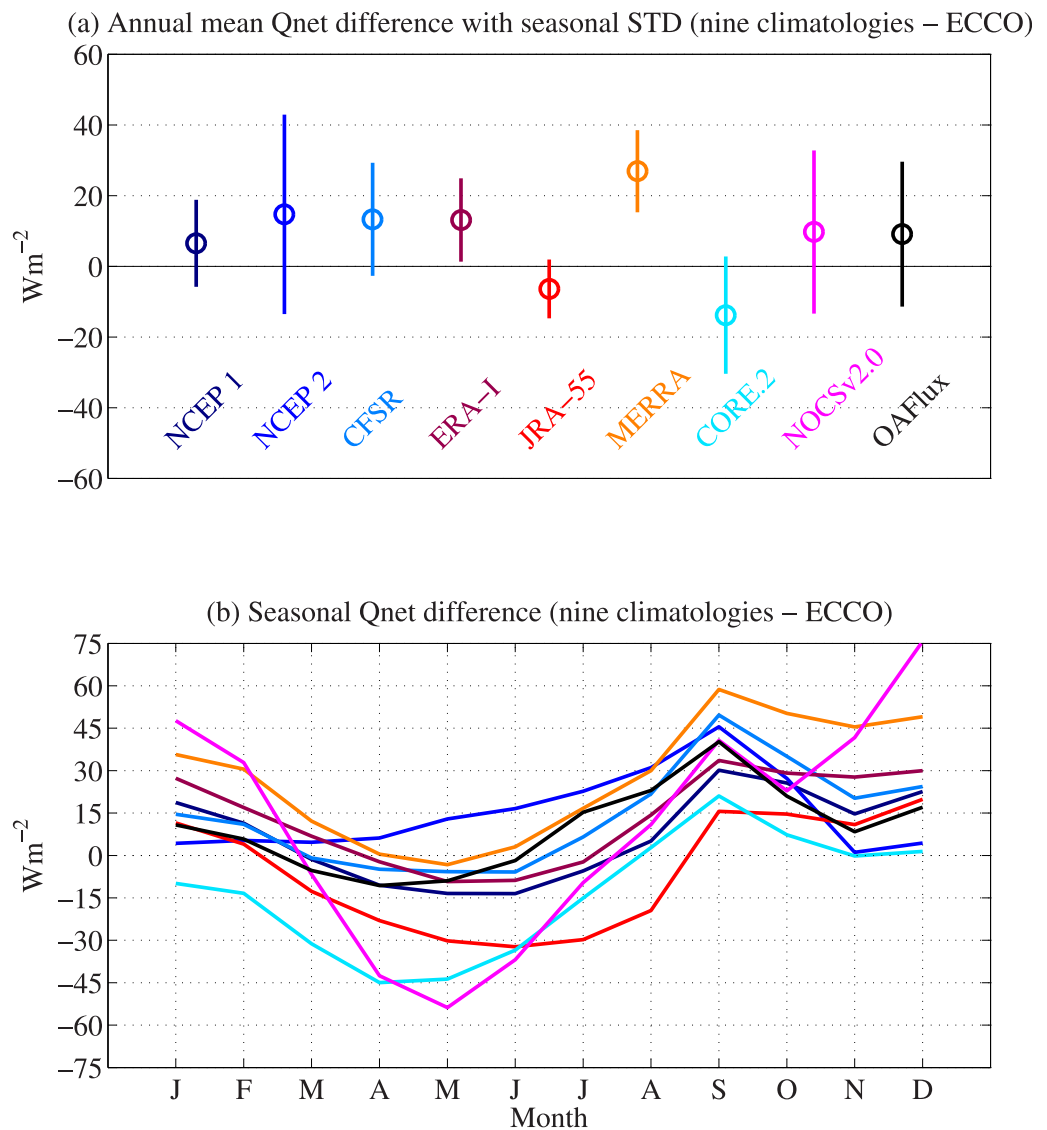(b) Seasonal Qnet difference (nine climatologies – ECCO)

Figure 8. (a) Annual mean differences between the nine Qnet climatologies and the reconstructed Qnet from WOA09. Error denotes the STD of seasonal deviations. (b) Seasonal Qnet differences between the nine Qnet climatologies and ECCO (e.g., OAFlux+ISCCP-ECCO, black).

2 ($+15$ W m^{-2}), CFSR ($+13$ W m^{-2}), ERA-Interim ($+13$ W m^{-2}), MERRA ($+27$ W m^{-2}), NOCSv2.0 ($+10$ W m^{-2}), and OAFlux+ISCCP ($+9$ W m^{-2}). A colder bias is obtained in JRA-55 (-6 W m^{-2}) and CORE.2 (-14 W m^{-2}) (Figure 8a). The STDs in Figure 8a evaluate the monthly deviation of Qnet differences. The maximum and the submaximum deviations are produced by NCEP 2 (±28 W m^{-2}) and NOCSv2.0 (±23 W m^{-2}). The minimum deviation is from JRA-55 (±8 W m^{-2}). The annual mean bias shows an overall warmer tendency in the Mediterranean Sea. Interestingly, in our previous warm pool work of SY13, the numbers of warm and cold products are nearly half and half.

The monthly differences are intercompared between nine Qnet climatologies and ECCO Qnet (e.g., OAFlux+ISCCP-ECCO, black, Figure 8b). All climatologies, except for NCEP 2, have a colder bias in warm season from May to July with respect to ECCO. All climatologies show a warm bias from September to February of the following year, with few exceptions of JRA-55 Qnet in September and CORE.2 Qnet in January and February. NOCSv2.0 has the largest warm bias at 76 W m^{-2} in September, and the largest cold bias at -54 W m^{-2} in March.
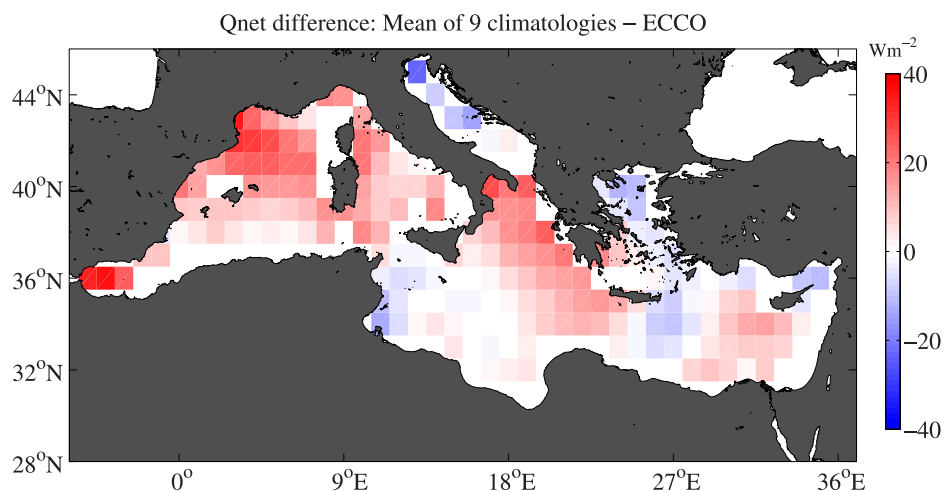
Figure 9. Spatial pattern of the annual-mean Qnet differences between the nine-product ensemble mean and ECCO (unit: W m^{-2}).

NCEP 2 has a 12 month warm bias than ECCO (Figure 8b). The warm bias is most pronounced from June to November, exceeding 46 W m^{-2} in October. The bias is small from December to May of the following year, with magnitude ranging from 1 W m^{-2} in December to 6 W m^{-2} in May. MERRA has an 11 month warm bias and is the warmest product, with magnitude reaching 59 W m^{-2} in December. Although most warm bias takes place over the whole year, MERRA performs better than the other eight climatologies from May to July. Some other products (CFSR, ERA-Interim, and OAFlux+ISCCP) have a 4 month colder bias and an 8 month warm bias (Figure 8b). NCEP 1 and NOCSv2.0 have a 5 month colder bias and a 7 month warm bias. JRA-55 and CORE.2 are cold biased, and they have an underestimated Qnet for more than 6 months.

The spatial structure of the Qnet differences between the nine-product ensemble mean and ECCO shows a basin-wide warm bias pattern with limited cold bias. The bias is most significantly in the northwestern Mediterranean Sea (Gulf of Lyon) and the Ionian Sea, while the cold bias is limited to coast regions, e.g., the Adriatic Sea and the Aegean Sea. The largest warm bias is 40 W m^{-2} in the Strait of Gibraltar, and the largest cold bias is -20 W m^{-2} in the north of Adriatic Sea. In the regions where the deep water forms, the ensemble mean Qnet is higher than ECCO, implying that the two sets of estimates would produce different rate of the deep water formation. The mean difference is 8 W m^{-2}, consistent with the estimation that the mean Qnet of nine climatologies is 2 W m^{-2}, and the mean Qnet of ECCO is -6 W m^{-2}.

5. Discussion and Conclusion

This study provides an analysis of the Mediterranean Sea surface energy budget using nine surface heat flux climatologies. The ensemble mean estimation shows that the net downward shortwave radiation (192 ± 19 W m^{-2}) is balanced by latent heat flux (-98 ± 10 W m^{-2}), followed by net longwave radiation (-78 ± 13 W m^{-2}) and sensible heat flux (-13 ± 4 W m^{-2}). The resulting net heat budget (Qnet) is 2 ± 12 W m^{-2} into the ocean, which appears to be warm biased. The annual-mean Qnet should be -5.6 ± 1.6 W m^{-2} when estimated from the observed net transport through the Strait of Gibraltar.

To diagnose the uncertainty in nine Qnet climatologies, we constructed Qnet from the heat budget equation by using historic hydrological observations to determine the heat content changes and advective heat flux. The heat budget analysis was conducted using the basin-integration of the heat budget equation (equation (2)). The heat budget closure is examined by estimating the heat content changes, advective heat flux across the Strait of Gibraltar, and the air-sea Qnet. On the annual mean basis, the mean heat content changes is required to be zero so that the along-strait advective heat flux should be balanced by the outgoing Qnet at the surface. On the seasonal timescales, however, the heat balance was achieved between the heat content changes and Qnet, as the advective heat flux was a small contribution. A mean Qnet was reconstructed using the hydrographic observations and the temperature climatologies, showing that the

annual-mean Qnet should be -5.6 ± 1.6 W m^{-2} and is significant at 95% confidence level. The reconstructed Qnet provides a physical constraint for evaluating the nine climatologies. Seven products (NCEP 1, NCEP 2, CFSR, ERA-Interim, MERRA, NOCSv2.0, and OAFlux+ISCCP) overestimate Qnet (warm bias) by as much as 6–27 W m^{-2}. Two climatologies underestimate Qnet (cold bias), with one (JRA-55) by -6 W m^{-2} and the other (CORE.2) by -14 W m^{-2} (CORE.2). We found that NCEP 1 and JRA-55 produce a reasonable climatological Qnet. This is different from our finding in the warm pool [SY13], where NCEP 1 has a large cold bias. By comparison, NOCSv2.0, MERRA, CFSR, and OAFlux+ISCCP is biased warm not only in the warm pool but also in the Mediterranean Sea, while CORE.2 is cold biased in both regions. For NCEP 1, 2, and ERA-Interim, they have a cold bias in the warm pool but a warm bias in Mediterranean Sea.

We also used the Qnet from a data-assimilated global ocean state estimation from ECCO as an additional reference. The mean Qnet in ECCO is -6 W m^{-2}, equivalent to the annual mean Qnet derived from WOA09. ECCO Qnet has a maximum at 166 W m^{-2} in June, which is 26 W m^{-2} higher than WOA09. It has a minimum at -186 W m^{-2} in December, which is 23 W m^{-2} lower than WOA09. The Qnet from ECCO is used to evaluating the nine climatologies. We found that NCEP 2 has a 12 month warm bias, and the other eight climatologies tend to overestimate Qnet in colder season from August to February of the following year, but underestimate Qnet from March to July. All the nine climatologies have a larger warm bias in September than other months.

We found that the threshold of the ratio, (SW+LW)/$-$LH, could be set to be 1.1 and used to obtain the right sign of Qnet. The signs and magnitudes of the nine Qnet climatologies are sensitive to this ratio. When (SW+LW)/$-$LH is less than 1.1 but greater than 1, the Qnet product shows a cold bias. If the ratio is greater than 1.1 but less than 1.2, the product has a small warm bias (i.e., less than 10 W m^{-2}). When the ratio is close to 1.4, the product (i.e., MERRA) has a large warm bias (exceeding 27 W m^{-2}).

This work is a continuation of our effort toward understanding and quantifying the uncertainties in the surface heat flux climatologies in the framework of ocean dynamics and heat budget balance. The main advantage of this approach is to use physical constraints to examine the uncertainties of Qnet. Together with our previous work in the warm pool [SY13], our study aims at a better understanding of the global air-sea heat flux closure. In this study, we pointed out that Qnet is overestimated in the nine climatologies in the northwestern Mediterranean Sea where the deep water forms. The mean Qnet in the Mediterranean Sea is overly overestimated in the colder seasons from September to December but underestimated from March to June. The net downward SW is overestimated in the boreal summertime when the SW is strong. We showed that higher resolution heat fluxes are desirable to capture the complex air-sea interactions near the coastal areas. These findings will be useful to help improve the present heat flux data sets and to improve our ability to estimate air-sea fluxes more accurately in numerical models and analyzed flux products. The current radiative transfer models for SW [*Tragou and Lascaratos*, 2003] and LW [*Fung et al.*, 1984] and bulk formulae for turbulent heat fluxes (LH+SH) [*Fairall et al.*, 2003] were found to differ in parameterizations. A study by *Song* [2012] has shown that, with the same input of physical parameters (e.g. SST, surface air temperature, humidity and cloud fraction), the net LW estimated by different radiative transfer models [*Fung et al.*, 1984] has a discrepancy of $\sim$60 W m^{-2} between the maximum and minimum calculations. We also felt the need for high-quality input of flux-related variables. The nine climatologies are obtained from different data sources, e.g., NOCSv2.0 is estimated from ship observations, OAFlux is an objective synthesis of satellite observations and atmospheric reanalyses. ISCCP is mostly satellite based. On the other hand, the atmospheric reanalysis is from the numerical simulations without an energy conservation at the surface. Different data resources have different errors, which affect the heat flux estimates.

Currently, new satellite surface radiation products that are developed by the Clouds and the Earth's Radiant Energy System (CERES) project at the NASA Langley represent a major improvement for quantifying the solar and longwave radiation at the top-of-atmosphere and at the Earth's surface [*Kato et al.*, 2013]. New turbulent heat flux products have also been constructed as a result of new retrieval algorithms and enhanced use of satellite observations from multiple platforms [e.g., *Jin et al.*, 2015]. Improved turbulent heat and momentum flux algorithms are also on the way [e.g., *Edson et al.*, 2013]. We anticipate major improvements in the surface flux estimates in the coming year, and hope that the improvement will help us to reconcile the differences in surface heat budgets on both regional and global scales.

References

Angelucci, M. G., N. Pinardi, and S. Castellari (1998), Air-sea fluxes from operational analysis fields: Intercomparison between ECMWF and NCEP analyses over the Mediterranean Sea, *Phys. Chem. Earth*, *23*, 569–574.

Bascheck, B., U. Send, J. G. Lafuente, and J. Candela (2001), Transport estimates in the Strait of Gibraltar with a tidal inverse model, *J. Geophys. Res.*, *106*(C12), 31,033–31,044.

Bentamy, A., K. B. Katsaros, A. M. Mestas-Nunez, W. M. Drennan, E. B. Forde, and H. Roquet (2003), Satellite estimate of wind speed and latent heat flux over the global oceans, *J. Clim.*, *10*, 637–656.

Berry, D. I., and E. C. Kent (2009), A new air-sea interaction gridded dataset from ICOADS with uncertainty estimates, *Bull. Am. Meteorol. Soc.*, *90*, 645–656.

Berry, D. I., and E. C. Kent (2011), Air-sea fluxes from ICOADS: The construction of a new gridded dataset with uncertainty estimates, *Int. J. Climatol.*, *31*, 987–1001, doi:10.1002/joc.2059.

Bethoux, J. (1979), Budgets of the Mediterranean Sea: Their dependence on the local climate and on the characteristics of the Atlantic waters, *Oceanol. Acta*, *2*, 157–163.

Bignami, F., S. Marullo, R. Santoleri, and M. E. Schiano (1995), Longwave radiation budget in the Mediterranean Sea, *J. Geophy. Res.*, *100*(C2), 2501–2514.

Bosilovich, M., et al. (2008), , Validation of NASA's Modern Era Retrospective-analysis for Research and Applications (MERRA), *Eos Trans. AGU*, *89*(23), Jt. Assem. Suppl., Abstract U41B-04.

Bryden, H. L., and H. M. Stommel (1984), Limiting processes that determine basic features of the circulation in the Mediterranean Sea, *Oceanol. Acta*, *7*, 289–296.

Bryden, H. L., and T. H. Kinder (1991), Steady two-layer exchange through the Strait of Gibraltar, *Deep Sea Res., Part A*, *38*, 445–463.

Bryden, H. L., et al. (1994). Exchange through the Strait of Gibraltar, *Prog. Oceanogr.*, *33*, 201–248.

Bunker, A. F. (1972), Wintertime interactions of the atmosphere with the Mediterranean Sea, *J. Phys. Oceanogr.*, *2*, 225–238.

Bunker, A. F., H. Charnock, and R. A. Goldsmith (1982), A note on the heat balance in the Mediterranean and Red Seas, *J. Mar. Res.*, *40*, 73–84.

Candela, J. (2001), The Mediterranean water and the global circulation, in *Observing and Modeling the Global Ocean*, edited by G. Siedler, J. Church, and J. Gould, pp. 419–429, Academic, San Diego, Calif.

Carton, J. A., and Z. Zhou (1997), Annual cycle of sea surface temperature in the tropical Atlantic Ocean, *J. Geophys. Res.*, *102*(C13), 27,813–27,824.

Castellari, S., N. Pinardi, and K. Leaman (1998), A model study of air-sea interactions in the Mediterranean Sea, *J. Mar. Syst.*, *18*, 89–114.

Chen, T., W. Rossow, and Y. Zhang (2000), Radiative effects of cloud-type variations, *J. Clim.*, *13*, 264–286.

Clark, N. E., L. Eber, R. M. Laurs, J. A. Renner, and J. F. T. Saur (1974), Heat exchange between ocean and atmosphere in the eastern North Pacific for 1961-71, *NOAA Tech. Rep. NMFS SSRF-682*, U.S. Dep. of Commer., Washington, D. C.

Dee, D. P., and S. Uppala (2009), Variational bias correction of satellite radiance data in the ERA-Interim reanalysis, *Q. J. R. Meteorol. Soc.*, *135*, 1830–1841.

Dee, D. P., et al. (2011), The ERA-Interim reanalysis: Configuration and performance of the data assimilation system, *Q. J. R. Meteorol. Soc.*, *137*, 553–597, doi:10.1002/qj.828.

DeLaughter, J. E., C. A. Stein, and S. Stein (2005), Hotspots: A view from the swells, *Spec. Pap. Geol. Soc. Am.*, *388*, 257–278.

Dietrich, D. E., R. L. Haney, V. Fernandez, S. Josey, and J. Tintore (2004), Air-sea fluxes based on observed annual cycle surface climatology and ocean model internal dynamics: A precise, non-damping zero-phase-lag approach applied to the Mediterranean Sea, *J. Mar. Syst.*, *52*, 145–165.

Edson, J. B., V. Jampana, R. A. Weller, S. P Bigorre, A. J. Plueddemann, and C. W. Fairall (2013), On the exchange of momentum over the open ocean, *J. Phys. Oceanogr.*, *43*(8), 1589–1610.

Fairall, C. W., E. F. Bradley, J. E. Hare, A. A. Grachev, and J. B. Edson (2003), Bulk parameterization on air–sea fluxes: Updates and verification for the COARE algorithm, *J. Clim.*, *16*, 571–591.

Fichaut, M., M. J. Garcia, A. Giorgetti, A. Iona, A. Kuznetsov, M. Rixen, and the MEDAR Group (2003), MEDAR/MEDATLAS 2002: A Mediterranean and black sea database for operational oceanography, *Elsevier Oceanogr. Ser.*, *69*(3), 645–648.

Foltz, G. R., J. Vialard, B. P. Kumar, and M. J. McPhaden (2010), Seasonal mixed layer heat balance of the southwestern tropical Indian Ocean, *J. Clim.*, *23*, 947–965.

Forget, G., J.-M. Campin, P. Heimbach, C. N. Hill, R. M. Ponte, and C. Wunsch (2015), ECCO version 4: An integrated framework for non-linear inverse modeling and global ocean state estimation, *Geosci. Model Dev.*, *8*, 3071–3104, doi:10.5194/gmd-8-3071-2015.

Fung, I. Y., D. E. Harrison, and A. A. Lacis (1984), On the variability of the net longwave radiation at the ocean surface, *Rev. Geophys.*, *22*(2), 177–193.

Garrett, C., R. Outerbridge, and K. Thompson (1993), Interannual variability in Mediterranean heat and buoyancy fluxes, *J. Clim.*, *6*, 900–910.

Gent, P. R., and J. C. McWilliams (1990), Isopycnal mixing in ocean circulation models, *J. Phys. Oceanogr.*, *20*, 150–155.

Gilman, C., and C. Garrett (1994), Heat flux parameterizations for the Mediterranean Sea: The role of atmospheric aerosols and constraints from the water budget, *J. Geophys. Res.*, *99*(C3), 5119–5134.

Hartmann, D. L., and D. Doelling (1991), On the net radiative effectiveness of clouds, *J. Geophys. Res.*, *96*(D1), 1204–1253.

Hellerman, S., and M. Rosenstein (1983), Normal monthly wind stress over the world ocean with error estimates, *J. Phys. Oceanogr.*, *13*, 1093–1104.

Jin, X., L. Yu, D. D. L. Jackson, and G. A. Wick (2015), An improved near-surface specific humidity and air temperature climatology for the SSM/I satellite period, *J. Atmos. Oceanic Technol.*, *32*, 412–433.

Josey, S., S. Gulev, and L. Yu (2013), Exchanges through the ocean surface, in *Ocean Circulation and Climate: A 21st Century Perspective, Int. Geophys.*, vol. 103, edited by G. Siedler et al., 2nd ed., pp. 115–140, Academic, Oxford, U. K.

Kalnay, E., et al. (1996), The NCEP/NCAR 40-year reanalysis project, *Bull. Am. Meteorol. Soc.*, *77*, 437–471.

Kanamitsu, M., et al. (2002), NCEP-DOE AMIP-II reanalysis (R-2), *Bull. Am. Meteorol. Soc.*, *83*(11), 1631–1643, doi:10.1175/BAMS-83-11-1631.

Kato, S., N. G. Loeb, F. G. Rose, D. R. Doelling, D. A. Rutan, T. E. Caldwell, L. Yu, and R. A. Weller (2013), Surface irradiances consistent with CERES-derived top-of-atmosphere shortwave and longwave irradiances, *J. Clim.*, *26*, 2719–2740.

Kobayashi, S., et al. (2015), The JRA-55 reanalysis: General specifications and basic characteristics, *J. Meteorol. Soc. Jpn.*, *93*(1), 5–48, doi:10.2151/jmsj.2015-001.

Krahmann, G., F. Schott, and U. Send (2000), Seasonal heat content changes in the western Mediterranean Sea as a means for evaluating surface heat flux formulations, *J. Geophys. Res.*, *105*(C7), 16,941–16,950.

Lafuente, J. G., J. Delgado, J. M. Vargas, M. Vargas, F. Plaza, and T. Sarhan (2002), Low frequency variability of the exchanged flows through the Strait of Gibraltar during CANIGO, *Deep Sea Res., Part II*, *49*, 4051–4067.

Large, W. G., and S. G. Yeager (2004), Diurnal to decadal global forcing for ocean and sea-ice models: The data sets and flux climatologies, *NCAR Tech. Note TN-4601STR*, 105 pp., NCAR Library, Boulder, Colo., doi:10.5065/D6KK98Q6.

Large, W. G., and S. G. Yeager (2009), The global climatology of an interannually varying air-sea flux data set, *Clim. Dyn.*, *33*, 341–364, doi: 10.1007/s00382-008-0441-3.

Locarnini, R. A., A. V. Mishonov, J. I. Antonov, T. P. Boyer, H. E. Garcia, O. K. Baranova, M. M. Zweng, and D. R. Johnson (2010), World ocean atlas 2009, volume 1: Temperature, in *NOAA Atlas NESDIS 68*, edited by S. Levitus, 184 pp., U.S. Gov. Print. Off., Washington, D. C.

MacDonald, A., J. Candela, and H. L. Bryden (1994), An estimate of the net heat transport through the strait of Gibraltar, in *Seasonal and Interannual Variability of the Western Mediterranean Sea, Coastal Estuarine Stud.*, vol. 46, edited by P. E. La Violette, pp. 13–32, AGU, Washington, D. C.

Madec, G., P. Delecluse, M. Crepon, and M. Chartier (1991), A three-dimensional numerical study of deep-water formation in the northwestern Mediterranean sea, *J. Phys. Oceanogr.*, *21*(9), 1349–1371.

Mariotti, A., M. V. Struglia, N. Zeng, and K. M. Lau (2002), The hydrological cycle in the Mediterranean region and implications for the water budget of the Mediterranean Sea, *J. Clim.*, *15*, 1674–1690.

Mariotti, A., N. Zeng, J. Yoon, V. Artale, A. Navarra, P. Alpert, and L. Li (2008), Mediterranean water cycle changes: Transition to drier 21st century conditions in the observations and CMIPs simulations, *Environ. Res. Lett.*, *3*, 044001, doi:10.1088/1748-9326/3/044001.

Matsoukas, C., A. C. Banks, N. Hatzianastassiou, K. G. Pavlakis, D. Hatzidimitriou, E. Drakakis, P. W. Stackhouse, and I. Vardavas (2005), Seasonal heat budget of the Mediterranean Sea, *J. Geophys. Res.*, *110*, C12008, doi:10.1029/2004JC002566.

May, P. W. (1982), Climatological flux estimates in the Mediterranean Sea, Part I: Winds and wind stress, *NORDA Rep. 54*, 57 pp., Nav. Ocean Res. and Dev. Activity, Stennis Space Cent., Miss.

MEDOC Group (1970), Observation of formation of deep water in the Mediterranean Sea, *Nature*, *227*, 1037–1040.

Nigam, S., and Y. Chao (1996), Evolution dynamics of tropical ocean–atmosphere annual cycle variability, *J. Clim.*, *9*, 3187–3205.

Petersen, G. N., and I. A. Renfrew (2009), Aircraft-based observations of air-sea fluxes over Denmark Strait and the Irminger Sea during high wind speed conditions, *Q. J. R. Meteorol. Soc.*, *135*, 2030–2045.

Pettenuzzo, D., W. G. Large, and N. Pinardi (2010), On the corrections of ERA-40 surface flux products consistent with the Mediterranean heat and water budgets and the connection between basin surface total heat flux and NAO, *J. Geophys. Res.*, *115*, C06022, doi:10.1029/2009JC05631.

Plakhin, Y. A. (1972), Vertical winter circulation in the Mediterranean, *Oceanology*, *12*, 344–351.

Ramanathan, V., R. D. Cess, E. F. Harrison, P. Minnis, B. R. Barkstrom, and E. Ahmad (1989), Cloud-radiative forcing and climate: Results from the earth radiation budget experiment, *Science*, *243*(4887), 57–63.

Ramanathan, V., B. Subasilar, G. J. Zhang, W. Conant, R. D. Cess, and J. T. Kiehl (1995), Warm pool heat budget and shortwave cloud forcing: A missing physics?. *Science*, *267*(5197), 499–503.

Reed, R. K. (1977), On estimating insolation over the oceans, *J. Phys. Oceanogr.*, *7*, 482–485.

Rienecker, M. M., et al. (2011), MERRA—NASA's modern-era retrospective analysis for research and applications, *J. Clim.*, *24*, 3624–3648.

Ruiz, S., D. Gomis, M. G. Sotillo, and S. A. Josey (2008), Characterization of surface heat fluxes in the Mediterranean Sea from a 44-year high-resolution atmospheric dataset, *Global Planetary Change*, *63*, 258–274.

Saha, S., et al. (2010), The NCEP climate forecast system reanalysis, *Bull. Am. Meteorol. Soc.*, *91*(8), 1015–1057, doi:10.1175/2010BAMS3001.1.

Samuel, S. L., K. Haines, S. A. Josey, and P. G. Myers (1999), Response of the Mediterranean Sea thermohaline circulation to observed changes in the winter wind stress field in the period 1980-1993, *J. Geophys. Res.*, *104*(C4), 7771–7784.

Sanchez-Gomez, E., S. Somot, S. A. Josey, C. Dubois, N. Elguindi, and M. Déqué (2011), Evaluation of Mediterranean Sea Water and heat budgets simulated by an ensemble of high resolution regional climate models, *Clim. Dyn.*, *37*, 2067–2086, doi:10.1007/s00382-011-1012-6.

Sankey, T. (1973), The formation of deep water in the northwestern Mediterranean, *Prog. Oceanogr.*, *6*, 159–179.

Schiano, M., R. Santoleri, F. Bignami, R. M. Leonardi, S. Marullo, and E. Bohm (1993), Air-sea interaction measurements in the West Mediterranean Sea during Tempo experiment, *J. Geophys. Res.*, *98*, 2461–2474.

Schiano, M. E. (1996), Insolation over the western Mediterranean Sea: A comparison of direct measurements and Reed's formula, *J. Geophys. Res.*, *101*(C2), 3831–3838.

Schulz, J., J. Meywerk, S. Ewald, and P. Schlussel (1997), Evalution of satellite-derived latent heat flux, *J. Clim.*, *10*, 2782–2795.

Song, X. (2012), Physical constraint on the air-sea heat flux based on the heat budget analysis, PhD thesis, 205 pp., Ocean Univ. of China, Qingdao, China.

Song, X., and L. Yu (2012), High-latitude contributions to global variability of air-sea sensible heat flux, *J. Clim.*, *25*, 3515–3531, doi:10.1175/JCLI-D-11-00028.1.

Song, X., and L. Yu (2013), How much net surface heat flux should go into the Western Pacific Warm Pool?, *J. Geophys. Res.*, *118*, 3569–3585, doi:10.1002/jgrc.20246.

Soto-Navarro, J., F. Criado-Aldeanueva, J. G. Lafuente, and A. Sanchez-Roman (2010), Estimation of the Atlantic inflow through the Strait of Gibraltar from climatological and in situ data, *J. Geophys. Res.*, *115*, C10023, doi:10.1029/2010JC006302.

Stein, C. A., and S. Stein (1992), A model for the global variation in oceanic depth and heat flow with lithospheric age, *Nature*, *359*, 123–129.

Stein, C. A., and S. Stein (1994), Comparison of plate and asthenospheric flow models for the thermal evolution of oceanic lithosphere, *Geophys. Res. Lett.*, *21*, 709–712.

Struglia, M. V., A. Mariotti, and A. Filograsso (2004), River discharge into the Mediterranean Sea: Climatology and aspects of the observed variability, *J. Clim.*, *17*, 4740–4751.

Sultan, S., A. James, and M. Collins (1987), Water masses in the northwestern Aegean, Eastern Mediterranean Sea (Autumn/Winter, 1978), *Thalassographica*, *10*(1), 89–104.

Tolmazin, D. (1985), Changing coastal oceanography of the Black Sea. Part II: Mediterranean effluent, *Prog. Oceanogr.*, *15*, 277–316, doi:10.1016/0079-6611(85)90039-4.

Tragou, E., and A. Lascaratos (2003), Role of aerosols on the Mediterranean solar radiation, *J. Geophys. Res.*, *108*(C2), 3025, doi:10.1029/2001JC001258.

Tsimplis, M. N., and H. L. Bryden (2000), Estimation of the transports through the Strait of Gibraltar, *Deep Sea Res., Part I*, *47*, 2219–2242.

Wunsch, C., and P. Heimbach (2007), Practical global ocean state estimation, *Physica D*, *230*, 197–208.

Yu, L. (2007), Global variations in oceanic evaporation (1958–2005): The role of the changing wind speed, *J. Clim.*, *20*, 5376–5390, doi:10.1175/2007JCLI1714.1.

Yu, L., and R. A. Weller (2007), Objectively analyzed air-sea heat fluxes for the global ice-free oceans (1981-2005), *Bull. Am. Meteorol. Soc.*, *88*(4), 527–539, doi:10.1175/BAMS-88-4-527.

Yu, L., X. Jin, and R. A. Weller (2008), Multidecade global flux datasets from the objectively analyzed air-sea fluxes (OAFlux) project: Latent and sensible heat fluxes, ocean evaporation, and related surface meteorological variables, *OAFlux Proj. Tech. Rep. OA-2008-01*, 64 pp., Woods Hole Oceanogr. Inst.

Yu, L., K. Haines, M. Bourassa, M. Cronin, S. Gulev, S. Josey, S. Kato, A. Kumar, T. Lee, and D. Roemmich (2013), Towards achieving global closure of ocean heat and freshwater budgets: Recommendations for advancing research in air-sea fluxes through collaborative activities, in *Report of the CLIVAR/GSOP/WHOI Workshop on Ocean Syntheses and Surface Flux*.

Zhang, Y., W. B. Rossow, A. A. Lacis, V. Oinas, and M. I. Mishchenko (2004), Calculation of radiative fluxes from the surface to top of atmosphere based on ISCCP and other global data sets: Refinements of the radiative transfer model and the input data, *J. Geophys. Res.*, *109*, D19105, doi:10.1029/2003JD004457.